AIAA Aviation Forum and ASCEND co-located Conference Proceedings
21 - 25 July 2025, Las Vegas, Nevada
AIAA AVIATION FORUM AND ASCEND 2025

10.2514/6.2025-3639

Design and Analysis of Tandem Wing Aircraft at Ultra-Low Reynolds Numbers in Cruise Condition

Yan Ren * Gecheng Zha †
CoFlow Jet, LLC.
www.coflowjet.com
4649 Ponce de Leon Blvd, Suite 306, Coral Gables
FL 33146, USA

Abstract

This paper numerically investigates the aerodynamic performance and efficiency of a tandem-wing aircraft utilizing a Deflected Slipstream (DS) CoFlow Jet (CFJ) airfoil configuration designed specifically for cruise flight on Mars, where achieving high lift and efficiency is critical due to the extremely low air density environment. The tandem-wing system consists of front and rear DS-CFJ wings, each equipped with propellers positioned in front of the wings. Computational analyses employ a 3D Reynolds-Averaged Navier-Stokes (RANS) solver with the Spalart–Allmaras turbulence model, featuring a third-order Weighted Essentially Non-Oscillatory (WENO) scheme for inviscid fluxes and second-order central differencing for viscous fluxes. The simulations are conducted at a Mach number of 0.17 and a Reynolds number of 39,410. The tandem configuration comprises a small front wing (17.5% area of the rear wing) and a larger rear wing, both sharing identical chord lengths. The front and rear wings have aspect ratios of 3.5 and 20, respectively, yielding an area-averaged aspect ratio of 17.54. Both wings use the DS-CFJ-NACA6421 airfoil but feature distinct optimized flap angles (front: $\beta = 15°$, rear: $\beta = 35°$) specifically selected for Martian flight conditions. Leveraging a Wing-Wing Interaction mechanism, previously described in [1], this configuration enhances aerodynamic efficiency while ensuring a compact design, essential due to the limited fuselage dimensions feasible on Mars.

The optimal aerodynamic efficiency for the complete aircraft is achieved at specific flap angles, resulting in a lift-to-drag ratio (C_L/C_D) of 10.35 and a corrected aerodynamic efficiency ($C_L/(C_D)_c$) of 5.37. These conditions yield an exceptionally high cruise lift coefficient (C_L) of 3.26, significantly surpassing conventional subsonic aircraft, which typically exhibit cruise lift coefficients below 0.6. This excellent aerodynamic performance, facilitated by CFJ active flow control, enables sustained flight beyond the limits of conventional aerodynamic technologies. The efficiency enhancement arises from favorable aerodynamic interactions between the tandem wings: the front wing's tip vortex positively augments lift on the rear wing, while the rear wing's high lift generation and increased circulation produce beneficial upwash that further boosts the front wing's efficiency. This innovative tandem wing configuration enabled by CFJ renders fixed wing VTOL aircraft feasible on Mars, although further studies are necessary for continued optimization.

To compare with conventional technology, the same aircraft is redesigned by replacing the DS-CFJ wing with a wing using NACA 6410 airfoil with the same aspect ratios, chords, and spans. The comparison indicates that conventional technology is not feasible to generate required cruise lift to support the weight of the structure.

Nomenclature

CFJ	Co-flow jet

---

[*] CoFlow Jet, LLC., CTO, Ph.D., AIAA member
[†] CoFlow Jet, LLC., President, AIAA Associate Fellow, Professor of the University of Miami

ρ	Air Density
$\dot{m}$	Mass Flow Rate
M	Mach Number
M_i	Isentropic Mach Number
Re	Reynolds Number
L	Aerodynamics Lift
D	Aerodynamic Drag
p	Static Pressure
p_0	Total Pressure
η	Pumping Power
q_∞	Freestream Dynamic Head, $\frac{1}{2}\rho_\infty {V_\infty}^2$
C_L	Lift Coefficient, $\frac{L}{q_\infty S}$
C_D	Drag Coefficient, $\frac{D}{q_\infty S}$
C_M	Moment Coefficient, $\frac{M}{q_\infty S c}$
C_p	Pressure Coefficient, $\frac{p-p_\infty}{q_\infty}$
C_μ	Jet Momentum Coefficient, $\frac{\dot{m}_j v_j}{q_\infty S}$
$(\frac{L}{D})$	Conventional Aerodynamic Efficiency
P_c	CFJ Power Coefficient, $\frac{P}{q_\infty S V_\infty}$
$(\frac{L}{D})_c$	Corrected Aerodynamic Efficiency for CFJ Airfoil, $\frac{L}{D+P/V_\infty} = \frac{C_L}{C_D+P_c}$
$(\frac{C_L^2}{C_D})$	Productivity Efficiency Coefficient
$(\frac{C_L^2}{C_D})_c$	Corrected Productivity Efficiency Coefficient for CFJ Airfoil
∞	Free Stream Conditions

1 Introduction

1.1 Fixed Wing Martian VTOL aircraft

The guideline of NRC [2] for space exploration indicates that "mobility is not just important for solar system exploration – it is essential". The case is exemplified for Mars, where spacecraft mobility would enable major advances in understanding climate change and geologic history and in searching for direct evidence of past life.

NASA has sent landers, rovers, a helicopter, and orbiters to Mars to perform various scientific missions. The rovers have the ability to examine surface samples, but the range is at a "point" scale compared with the vast area of Martian surface. The orbiters do have a global scale range, but the high altitude limits the observation resolution and there is no capability to examine near surface atmosphere and ground samples. The recent great success of solar powered Ingenuity helicopter opens an era of aircraft flying on another planet. Since landed on Mars over in Feb. 2021, Ingenuity had traveled 11.7 km before it ceased functioning in January 2024. Even though the range is short, it has inspired our journey to develop Martian aircraft as a global scale explorer near and on Martian surface.

A global scale aircraft on Mars needs to have the following crucial features: 1) vertical takeoff and land (VTOL) to examine the air and soil; 2) light weight, high efficiency with long range and high payload for scientific equipment; 3) sustainable and self-sufficient in energy. Such an aircraft could be a scaled up Ingenuity helicopter. However, a fixed wing VTOL aircraft is more efficient to fly for a long range and high payload. A fixed wing aircraft can also integrate the solar panel with its wings to be aerodynamically and structurally efficient. Helicopter can not put solar panels on the rotating propeller blades due to high centrifugal load. Ingenuity has a dedicated solar panel on top of the propeller. Such a configuration would be difficult to scale up and will penalize the mission efficiency significantly. However, a conventional fixed wing aircraft cruising at a lift coefficient C_L of 0.4-0.6 would be very difficult to fly on Mars with a significant payload. It would require a very large wing surface with heavy weight penalty due to the low Martian atmospheric density. It must fly fast to avoid an excessive wing size. For example, NASA's ARES concept (Aerial Regional-scale Environmental Survey of Mars)[3] is designed to fly at Mach 0.65 powered by a rocket engine. Such a high speed is acceptable for a "one-shot" flight, but is extremely difficult to achieve energy self-sufficiency using solar energy on Mars because the energy required is proportional to the square of flight speed for a fixed distance. The other difficulty in flying on Mars is the low Reynolds number, which makes flow prone to be separated and substantially reduces aerodynamic efficiency and operating range due to stall.

This paper is to conduct a study for a proposed Martian fixed wing VTOL aircraft MAGGIE (Mars Aerial and Ground Global Intelligent Explorer) at cruise condition using deflected slipstream enabled by CoFlow Jet (CFJ) active flow control. MAGGIE provides unique and superior performance to fly on Mars globally utilizing sustainable solar energy[4].

1.2 Deflected Slipstream Enabled by CoFlow Jet

For VTOL aircraft, the deflected slipstream (DS) concept [5, 6, 7] generates hover lift by deflecting the horizontal slipstream from the forward facing propellers downward using a deflected flap. Once airborne, the flap is retracted for high-speed cruise. A 90° deflected slipstream would generate a pure vertical lift[8]. A functional DS aircraft would not use tiltwings, tiltrotors or lift-plus configurations, which would be used only at hover of takeoff and landing, but need to be carried for the entire mission with weight and drag penalty. However, extensive flow separation would occur when the flap deflection angle is large. Although the 10-year efforts to develop DS technology were abandoned in 1960's due to insufficient flow turning even with the double-slotted flaps [6], NASA recently revisited the DS concept and suggested using CoFlow Jet (CFJ) flow control to enhance the flow turning[9]. Experimental testing is conducted to demonstrate the slipstream deflection capability by implementing CFJ on the flap[10].

1.3 The Co-Flow Jet Active Flow Control Airfoil

The CFJ airfoil has an injection slot near the leading edge(LE) and a suction slot near the trailing edge(TE) on the airfoil suction surface as sketched in Fig. 1. A small amount of mass flow is withdrawn into the airfoil near the TE, pressurized and energized by a micro-compressor system inside the airfoil, and then injected near the LE in the direction tangent to the main flow. The whole process does not add any mass flow to the system and hence is a zero-net mass-flux flow control.

The CFJ airfoil flow control mechanism achieves a radical lift augmentation, drag reduction and stall margin increase at a very low energy expenditure. It can not only achieve ultra-high lift coefficient, but also significantly enhance cruise productivity efficiency and cruise wing loading from subsonic to transonic conditions[11, 12, 13, 14, 15, 16].

Yang and Zha [15] discovered in 2017 that a CFJ airfoil can achieve Super-Lift Coefficient(SLC), which is a lift coefficient that exceeds the theoretical limit of potential flow developed by Smith[17] and is defined below:

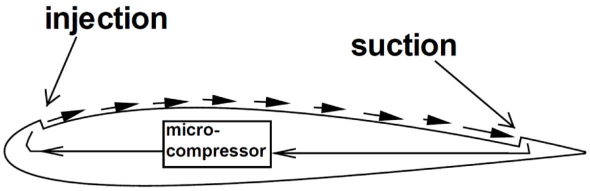

Figure 1: Baseline airfoil and CFJ Airfoil.

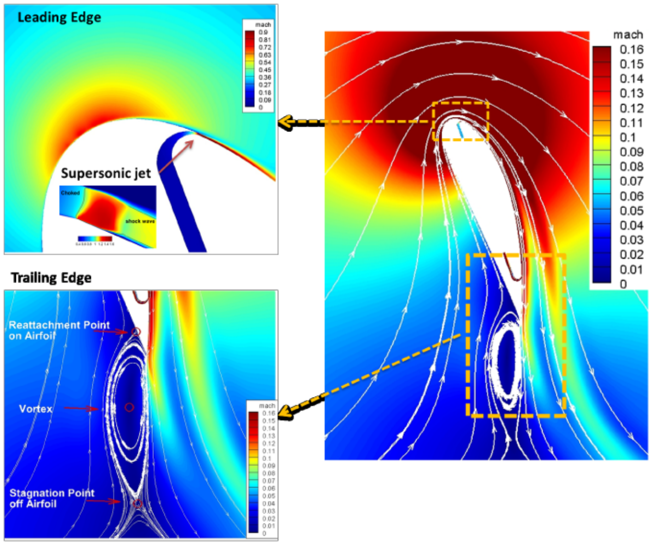

Figure 2: Mach number contours and streamlines at $C_\mu = 0.35$ and AoA $=70°$ for the CFJ6421-SST016-SUC053-INJ009 airfoil.

$$C_{Lmax} = 2\pi(1 + \frac{t}{c}) \tag{1}$$

When a SLC occurs, the circulation is so high that the stagnation point is detached from the airfoil body as shown in Fig. 2, which has a C_{Lmax} of 10.6, far greater than the theoretical limit of 7.6. The flow remains attached at AoA of 70° and the wake is filled with reversed velocity deficit, similar to the owl effect that generates very low wake turbulent noise. The CFJ airfoil pressure coefficient at the leading edge suction peak is nearly 10 times higher than the maximum value of the baseline airfoil at AoA of 18° before it stalls [15]. In other words, the CFJ airfoil at SLC condition can keep flow attached despite an adverse pressure gradient nearly one order of magnitude higher than the conventional airfoil. The simulation of Yang and Zha [15] also reveals a complex phenomenon with 4 layers of counter-rotating vortex layers emanating from leading edge and trailing to the wake of the airfoil. The detailed analysis can be seen in [15, 18].

2 MAGGIE's Configuration

MAGGIE is a tailless VTOL aircraft with a long wing in the rear and a canard in the front cruising at Mach number 0.17 (41.2 m/s) at an altitude of 1000 m. Fig. 3 shows MAGGIE's configuration at cruise with a thick-flapped CFJ-NACA-6421, which utilizes a simple hinge to control the plain CFJ flap that has a length of 60% chord. At hover, the flap turns the slipstream from the propellers 90° downward by deflecting the flap 75° . For cruise, the flap deflection angle, β, will be reduced to 15° for the front wing and 35° for the rear wing respectively as shown in Fig. 3. Such a configuration is optimized for system benefit to harvest the energy of the tip vortex of the front wing and the up-wash of the rear wing to be explained later. For flight control, the flap on each side of the wing will have multiple segments along the span to provide effective pitching and rolling control. For yaw control, multiple propellers and micro-compressor actuators embedded inside the flaps are control actuators together with the flaps [19, 20]. The large number of propellers and micro-compressor actuators also provide high redundancy to increase the operation reliability. This paper is to conduct the preliminary design and analysis of MAGGIE aircraft at cruise.

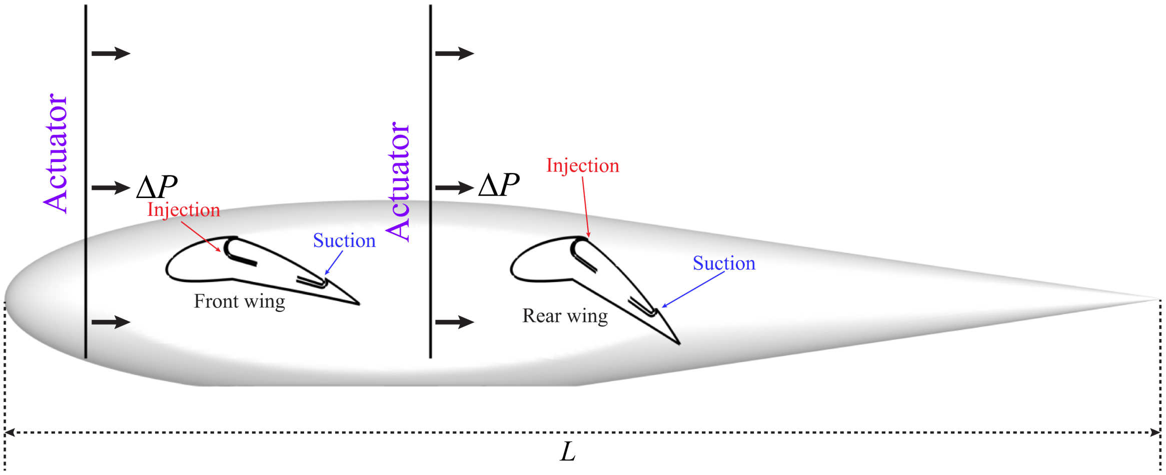

Figure 3: Side view of the tandem wing air vehicle with propellers mounted above the wings.

3 Methodology

3.1 Tandem Wing Propeller-CFJ Parameters

The parameters used to define the tandem wing propeller-CFJ system are described in this section.

The injection jet momentum coefficient C_μ is used to describe the CFJ strength as:

$$C_\mu = \frac{\dot{m} V_j}{\frac{1}{2}\rho_\infty {V_\infty}^2 S} \tag{2}$$

where $\dot{m}$ is the injection mass flow, V_j is the mass-averaged injection velocity, ρ_∞ and V_∞ denote the free stream density and velocity, and S is the airfoil planform area.

The conventional airfoil aerodynamic efficiency is defined as

$$(\frac{L}{D}) = \frac{C_L}{C_D} \tag{3}$$

For CFJ wing, the ratio above represents the pure aerodynamic relationship between lift and drag. Taking into account the energy consumption of the CFJ, the conventional aerodynamic efficiency is modified by converting the power consumption into a corresponding drag force. The equation of the corrected aerodynamic efficiency is given as the following[13]

$$(\frac{L}{D})_c = \frac{L}{D + \frac{P}{V_\infty}} \tag{4}$$

in which the CFJ pumping power consumption P is converted into a force $\frac{P}{V_\infty}$ added to the aerodynamic drag D. The formulation above can be further expressed using the non-dimensional coefficients C_L, C_D and P_c as

$$(\frac{C_L}{C_D})_c = \frac{C_L}{C_D + P_c} \tag{5}$$

Note that when the pumping power is set to 0, $(\frac{L}{D})_c$ returns to conventional aerodynamic efficiency definition. The C_L and C_D calculation needs to include the CFJ reactionary force as described by Zha et al [21].

The CFJ power required is determined by the total enthalpy rise from the suction duct outlet to the injection duct inlet[13]. The total enthalpy rise can be achieved by the embedded micro-compressors. The power required by the CFJ (P) can be expressed as:

$$P = \frac{\dot{m} H_{t2}}{\eta}(\Gamma^{\frac{\gamma-1}{\gamma}} - 1) \tag{6}$$

where γ is the specific heat ratio, Γ the total pressure ratio of the micro-compressor, H_{t2} the total enthalpy at the compressor inlet, $\dot{m}$ the jet mass flow rate, η the micro-compressor efficiency and is taken at 100% to compute the required power.

Eq. (6) indicates that the power required for CFJ is linearly determined by the mass flow rate and exponentially by the total pressure ratio. This relationship in fact applies to all the active flow controls based on fluidic actuators. Thus, C_μ should not be used to represent the power consumption of active flow control[13, 22]. For example, a high C_μ could have a substantially lower power consumption than a smaller C_μ if the high C_μ is created by a large mass flow rate and low jet velocity, which needs a significantly lower total pressure ratio[22, 23]. Yang and Zha[15] find that the only parameter correlated well with the maximum lift coefficient of CFJ airfoil is the power coefficient defined below:

$$P_c = \frac{P}{\frac{1}{2}\rho_\infty V_\infty^3 S} \tag{7}$$

where P is the CFJ required power defined in Eq. 6.

The transportation capability of an airplane is measured by how much total weight the aircraft can move for the maximum distance. In Yang et. al (2017)[15], a term "productivity" is defined as the product of the total weight by the maximum range to represent the transportation capability of an airplane.

For a jet engine airplane, the total weight of the aircraft decreases during flight. A non-dimensional productivity parameter is hence defined using the aircraft averaged weight as below:

$$C_{RW} = \frac{R\overline{W}}{\frac{1}{2c_t}\bar{\rho} V_\infty^3 S} = \frac{C_L^2}{C_D} \ln \frac{W_0}{W_f} \tag{8}$$

where R is the aircraft range, $\overline{W}$ is the averaged weight of the aircraft during cruise, c_t is the engine cruise thrust specific fuel consumption[fuel weight(N)/(thrust(N) s)], $\bar{\rho}$ is the averaged air density during cruise due to altitude variation, S is the wing platform area, W_0 is the aircraft initial gross weight at takeoff, W_f is the final weight at landing. This formulation is obtained from the Breguet Range Equation. The productivity parameter represents the productivity of the aircraft with the fuel consumed per unit time.

For a full electric battery powered propeller airplane, the aircraft weight will not change during flight. The productivity parameter is defined as:

$$C_{RW} = \frac{RW}{\frac{1}{2}\rho V_\infty^2 S E_c/g} = \eta \frac{C_L^2}{C_D}\frac{W_b}{W_0} \tag{9}$$

where E_c is the battery specific energy density (Wh/kg), W_b is the total battery weight, W_0 is the gross weight, η is the propulsion system efficiency (e.g. propeller).

Clearly, both Eq. (8) and (9) indicate that the productivity parameter is determined by C_L^2/C_D, which is thus defined as productivity efficiency. The productivity efficiency is considered as a more comprehensive parameter than the conventional aerodynamic efficiency C_L/C_D to measure the merit of an airplane aerodynamic design for cruise performance. The former includes not only the information of C_L/C_D, but also the information of the aircraft weight represented by C_L.

For CFJ airfoil, the productivity efficiency should also include the CFJ power consumption and is defined as below:

$$\frac{C_L^2}{C_{Dc}} = \frac{C_L^2}{C_D + P_C} \tag{10}$$

This study involves a tandem wing configuration. For example, the coefficient of lift for each wing can be defined individually as:

$$C_{L1} = \frac{L_1}{\frac{1}{2}\rho_\infty {V_\infty}^2 S_1}, \quad C_{L2} = \frac{L_2}{\frac{1}{2}\rho_\infty {V_\infty}^2 S_2}, \tag{11}$$

where the subscript 1 and 2 stand for the first and second wing. For the aircraft system with tandem wings, the system lift coefficient is defined as the total lift based on the total wing area below:

$$C_{Lt} = \frac{L_1 + L_2}{\frac{1}{2}\rho_\infty {V_\infty}^2 (S_1 + S_2)} \tag{12}$$

where the subscript t stands for tandem wing.

Substituting Eq. (11) to Eq. (12), the system lift coefficient can be expressed as:

$$C_{Lt} = \frac{C_{L1}S_1 + C_{L2}S_2}{S_1 + S_2} \tag{13}$$

Eq. (13) is actually the same as the area weighted lift coefficient. Similarly, the coefficient of system drag and CFJ power can be defined as:

$$C_{Dt} = \frac{C_{D1}S_1 + C_{D2}S_2}{S_1 + S_2} \tag{14}$$

$$P_{ct} = \frac{P_{c1}S_1 + P_{c2}S_2}{S_1 + S_2} \tag{15}$$

The corrected drag coefficient is:

$$(C_{Dc})_t = C_{Dt} + P_{ct} \tag{16}$$

The aerodynamic efficiency and the productivity efficiency of the tandem wing system then can be defined following the same way as Eq. (5) and Eq. (10). To see the relations clearly, we take the aerodynamic efficiency of the tandem wing as an example below:

$$(\frac{L}{D_c})_t = \frac{L_1 + L_2}{D_1 + D_2 + P_1/V_\infty + P_2/V_\infty} = \frac{C_{Lt}\frac{1}{2}\rho_\infty {V_\infty}^2(S_1 + S_2)}{C_{Dt}\frac{1}{2}\rho_\infty {V_\infty}^2(S_1 + S_2) + P_{ct}\frac{1}{2}\rho_\infty {V_\infty}^2(S_1 + S_2)}$$

$$= \frac{S_1 C_{L1} + S_2 C_{L2}}{S_1 C_{D1} + S_2 C_{D2} + S_1 P_{c1} + S_2 P_{c2}} \tag{17}$$

That is:

$$(\frac{L}{D_c})_t = \frac{C_{Lt}}{(C_{Dc})_t} \tag{18}$$

3.2 CFD Simulation Setup

The in house FASIP (Flow-Acoustics-Structure Interaction Package) CFD code is used to conduct the numerical simulation. The simulations employ 3D RANS solver with Spalart-Allmaras (S-A) turbulence model. A 3rd order WENO scheme for the inviscid flux [24, 25, 26, 27, 28, 29] and a 2nd order central differencing for the viscous terms [24, 28] are employed to discretize the Navier-Stokes equations. The low diffusion E-CUSP scheme used as the approximate Riemann solver suggested by Zha et al [25] is utilized with the WENO scheme to evaluate the inviscid fluxes. Implicit time marching method using Gauss-Seidel line relaxation is used to achieve a fast convergence rate [30]. Parallel computing is implemented to save wall clock simulation time [31].

3.3 Boundary Conditions

The 3rd order accuracy no slip condition is enforced on the solid surface with the wall treatment suggested in [32] to achieve the flux conservation on the wall. The computational mesh is shown in Fig. 4. Total pressure, total temperature and flow angles are specified at the CFJ injection duct inlet, as well as the upstream portion of the far field. Constant static pressure is applied at the suction duct outlet as well as the downstream portion of the far field. The total mesh size is about 15 million, split into 241 blocks for the parallel computation. The computational domain is about 150 chords in the main stream direction and 50 chords in wing span direction to ensure an accurate simulation. The first grid point on the wing surface is placed at $y^+ \approx 1$. The propeller is simulated using an actuator disk boundary condition with a pressure jump (ΔP) imposed. The pressure jump is given as a percentage of the pressure upstream of the actuator, typically is fairly small and rarely greater than 2%. The pressure jump condition is very well handled by the Riemann solver employed in the FASIP CFD code. In this study, the ΔP for each propeller actuator disk is iterated to make the system resultant force in the flight direction to be zero for the cruise condition.

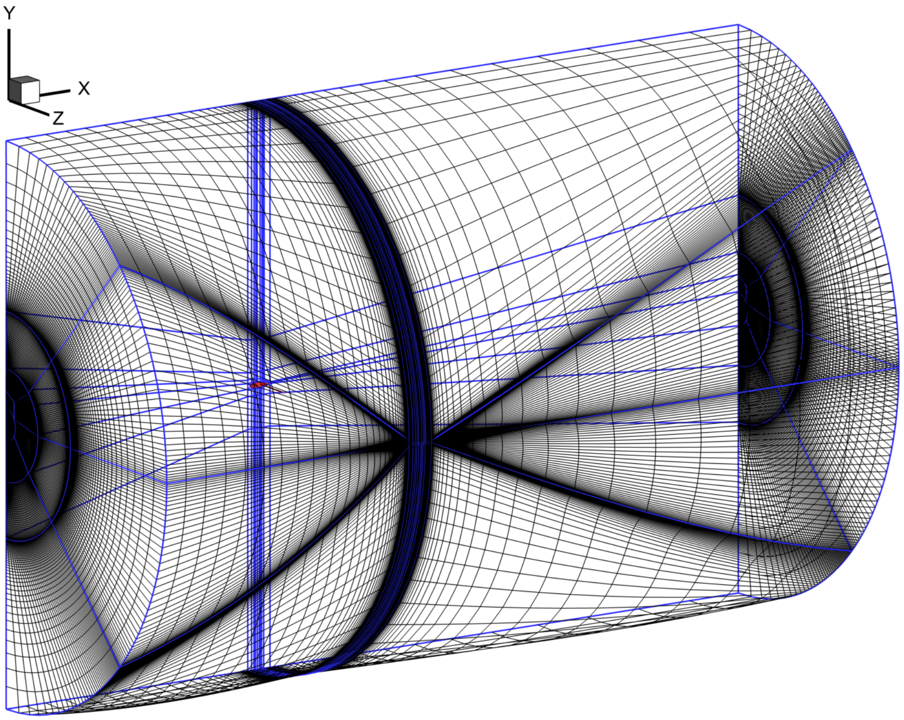

Figure 4: Computational mesh used in the current work.

4 Results

4.1 DS-CFJ aircraft cruise in Martian atmosphere

The results for the tandem wing aircraft with DS-CFJ technology focus on analyzing the optimized aircraft geometry (Fig. 5) designed for Martian flight. This configuration features front and rear DS wings with flap angles of 15° and 35°, respectively, and incorporates propellers mounted in front of both wings. The simulation is conducted under Martian atmospheric conditions, characterized by extremely low air density, a Mach number of 0.17, and a Reynolds number of 39410, necessitating an efficient lift-enhancing mechanism to achieve sustainable flight. Some key simulation parameters are listed in Table 1. The dimension of the aircraft is designed to fit to the payload faring of launch rockets with no wing folding required.

We first examine the 3D flow field around the tandem wing configuration, highlighting key flow phenomena such as vortex interactions, upwash regions, and flow control effects of the DS-CFJ system. Following this, we present the aerodynamic performance of the optimized configuration, evaluating both the lift and drag characteristics as well as the overall efficiency in terms of the corrected lift-to-drag ratio.

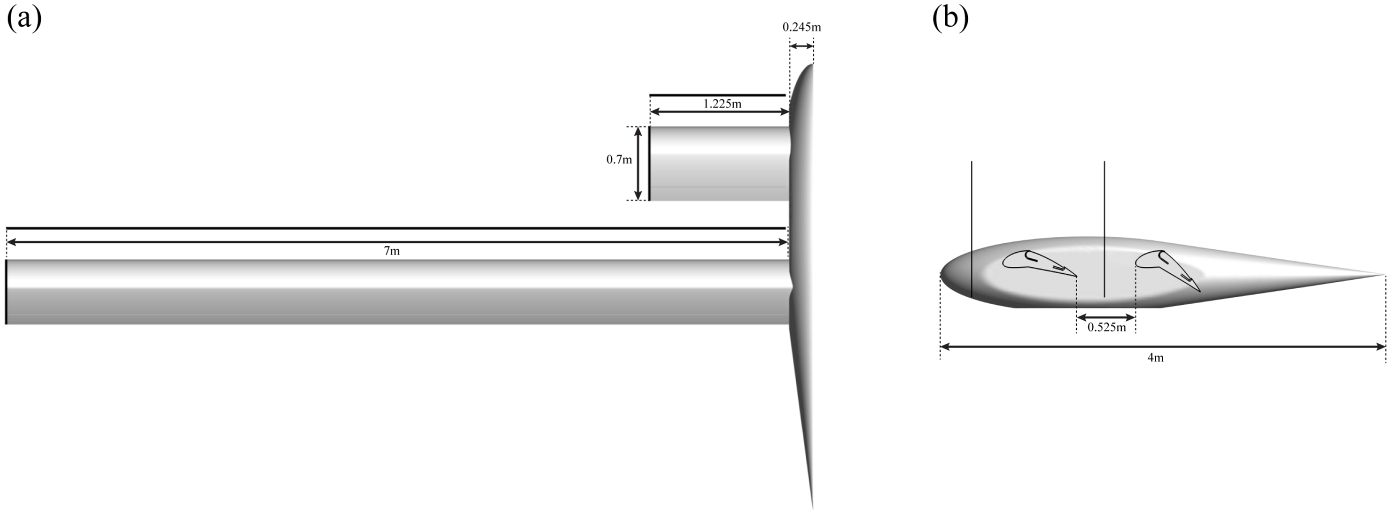

Figure 5: The top view (a) and side view (b) of the DS-CFJ aircraft in the current study.

Table 1: Simulation parameters used in the current study.

Component	AR	β	ΔP (%)	M_∞	C_μ
Front Wing	3.5	15°	0.3842	0.17	0.06
Rear Wing	20	35°			0.14
Full Aircraft	17.54	-			-

Fig. 6 (a) illustrates the vorticity iso-surface wake structures surrounding the aircraft wings. The roll-up vortex tubes originating from the wing tips distinctly highlight the tip vortices generated by both the front and rear wings. Notably, the rear wing's tip vortex exhibits greater strength due to the higher lift coefficient induced by the large flap angle, β. The propagation of the front wing's tip vortex downstream and its subsequent interaction with the rear wing are evident. This interaction results in the front wing tip vortex firmly attaching to the suction surface of the rear wing, showcasing a complex interplay between the two vortex systems.

Fig. 6 (b) depicts seven flow field slices, spanning from $z = 0.35\,\text{m}$ to $z = 7.2\,\text{m}$, with Mach contours representing the flow characteristics. The flow attachment is observed to be well-maintained across most regions. For the front wing, a smaller high-speed region and the absence of a low-speed region indicate reduced lift production but significantly higher aerodynamic efficiency. In contrast, the rear wing exhibits a larger high-speed region near the leading edge, which remains pronounced even in areas subjected to the wake of the front wing. This region corresponds to the interaction point where the front wing tip vortex impacts the rear wing.

The front wing tip vortex is lifted upward by the low-pressure region on the suction surface of the rear wing, generating an upwash effect that benefits both the front and rear wings. The magnitude of the upwash effect increases with the rear wing's flap angle β, which can be attributed to the large circulation induced by the rear wing. Additionally, the combined effects of the propellers and the CFJ at $C_\mu = 0.14$ facilitate flow attachment for the rear wing, even at a flap angle as high as $\beta = 35°$.

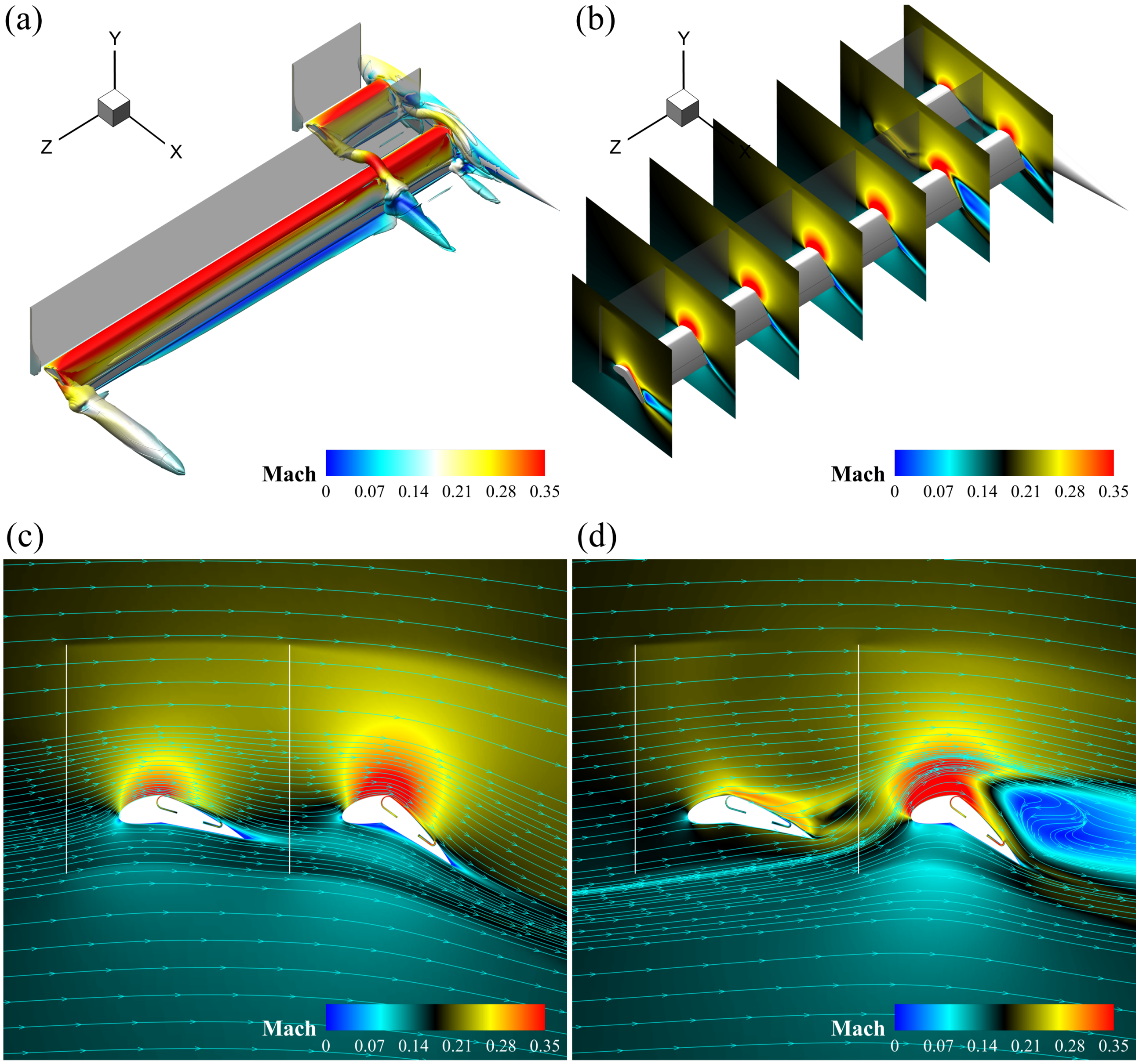

Figure 6: (a) The wake structures represented by the vorticity iso-surface (colored by Mach nubmer); (b) flow slices along the aircraft wings; (c) flow slice at $z = 0.8785m$; (d) flow slice at $z = 1.45m$.

Fig. 6 (c) and (d) illustrate flow slices with Mach contours and streamlines at $z = 0.8785\,\text{m}$ (mid-span of the front wing) and $z = 1.45\,\text{m}$ (front wing tip region), respectively. In Fig. 6 (c), the flow remains well-attached, with no evidence of flow separation observed. In contrast, Fig. 6 (d) demonstrates flow separation along the suction surface of the rear wing, caused by the tip vortex from the front wing. Nevertheless, an expanded high-speed region is observed over the rear wing, signifying enhanced lift generation. The aerodynamic coupling between the wings significantly enhances the efficiency of the front wing and augments the lift of the rear wing, albeit at the expense of a reduction in its aerodynamic efficiency. Overall, the wing–wing interaction leads to a net improvement in both total lift and aerodynamic efficiency of the tandem-wing system.

Table 2 summarizes the quantitative aerodynamic performance metrics for the cruise case. A high aircraft lift coefficient of 3.256 is achieved. The corrected aerodynamic efficiency, represented as C_L/C_{Dc}, is 8.438 for the front wing and 5.049 for the rear wing. For the full aircraft, the corrected aerodynamic efficiency is calculated as $C_L/C_{Dc} = 5.366$, and a net lift to drag ratio C_L/C_D of 10.34. These results yield a productivity efficiency C_L^2/C_{Dc} of 17.47. Such excellent overall aerodynamic performance and efficiency at cruise are essential for MAGGIE to perform the science missions on Mars.

Table 2: Aerodynamic performance for different body components of the DS-CFJ aircraft in cruise. The fuselage C_L and C_D are normalized by $S_1 + S_2$.

Body	AR	C_L	C_D	P_C	C_μ	C_L/C_D	C_L/C_{Dc}
FL	-	0.1182	0.0087	-	-	13.6144	-
FW	3.5	2.0889	0.1388	0.1088	0.06	15.0519	8.4377
RW	20	3.5406	0.3566	0.3446	0.14	9.9277	5.0492
TT	17.54	3.2557	0.3146	0.2921	-	10.3472	5.3662

4.2 Conventional baseline aircraft cruise in Martian atmosphere

To compare with conventional technology, the same aircraft using DS-CFJ is redesigned for the wings using NACA 6410 airfoil with the same aspect ratios, chords, and spans. For such a low Reynolds number, very thin airfoil (i.e. $1\% - 5\%$) is preferred. The NACA 6410 airfoil is selected to consider both the aerodynamic efficiency and structure integrity. Fig. 7 depicts the side view of the aircraft configuration. Key simulation parameters for the baseline aircraft are summarized in Table 3.

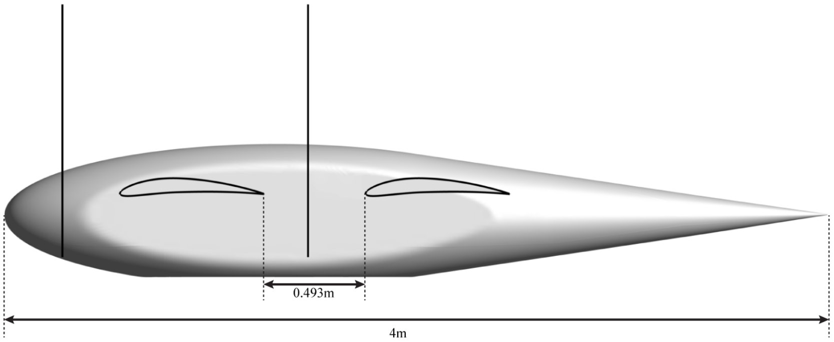

Figure 7: The side view of the baseline aircraft in the current study.

Table 3: Simulation parameters used in the current study of the baseline aircraft in cruise.

Component	AR	AoA	ΔP (%)	M_∞
Front Wing	3.5	4°	0.0391	0.17
Rear Wing	20	4°		
Full Aircraft	17.54	-		

Fig. 8 (a) illustrates the vorticity iso-surface wake structures around the baseline aircraft wings. Small wing tip vortices can be observed for both the front and rear wings. Additionally, the front wing tip vortex propagates downstream and interacts with the rear wing.

Fig. 8 (b) presents seven flow field slices, ranging from $z = 0.35\,\text{m}$ to $z = 7.2\,\text{m}$, colored by Mach contours. The flow attachment is observed to be very good; however, the high-speed region is smaller and weaker compared to that of the MAGGIE aircraft, indicating significantly lower lift production.

Fig. 8 (c) and (d) display flow slices with Mach contours and streamlines at $z = 0.8785\,\mathrm{m}$ (mid-span of the front wing) and $z = 1.45\,\mathrm{m}$ (front wing tip region), respectively. Both figures show a small and weak high-speed region alongside excellent flow attachment. These characteristics suggest limited lift production but high aerodynamic efficiency.

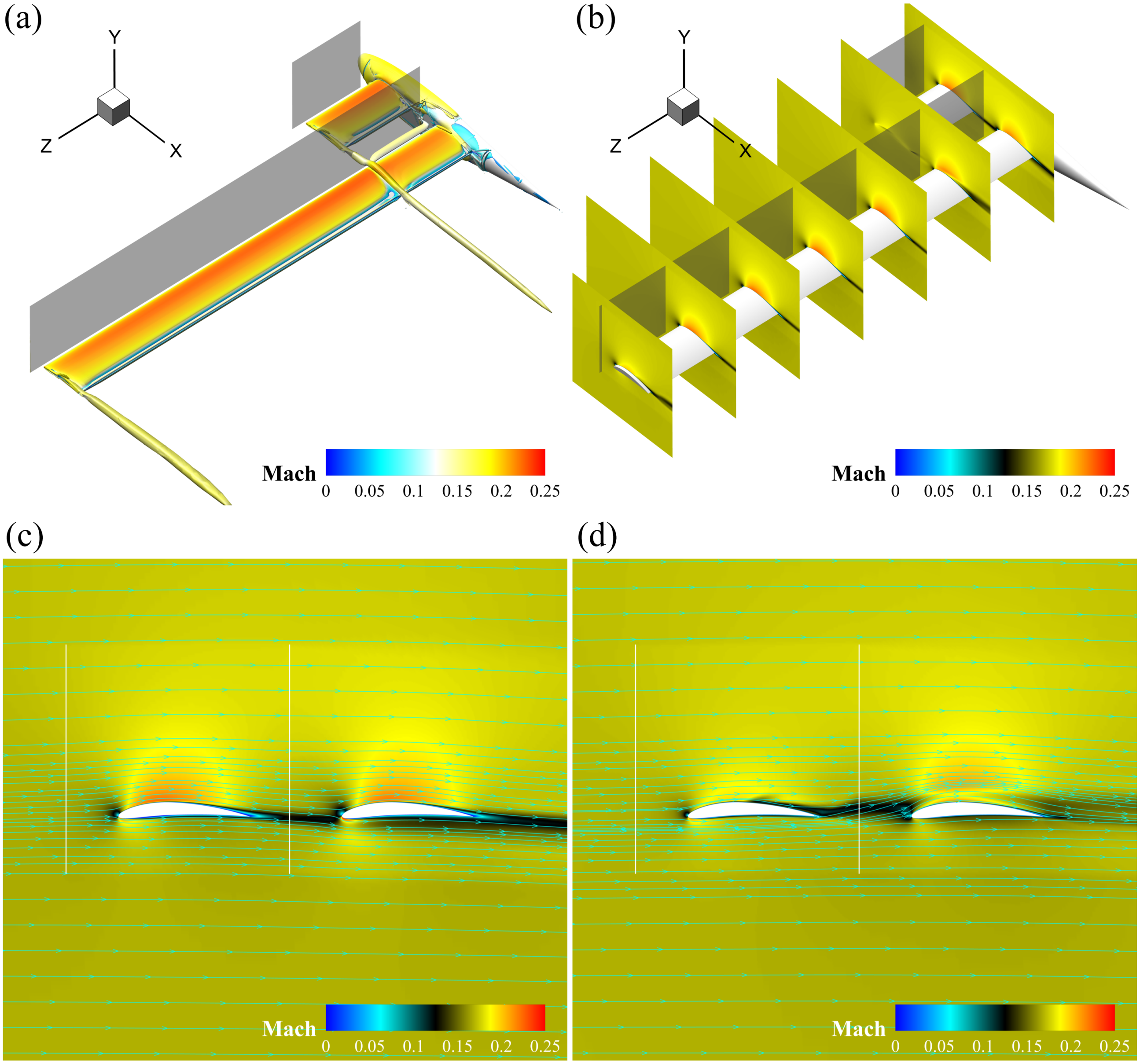

Figure 8: (a) The wake structures represented by the vorticity iso-surface (colored by Mach nubmer); (b) flow slices along the baseline aircraft wings; (c) flow slice at $z = 0.8785m$; (d) flow slice at $z = 1.45m$.

Table 4 summarizes the quantitative aerodynamic performance of the baseline aircraft. A relatively small lift coefficient of 0.431 is achieved. The aerodynamic efficiency, expressed as C_L/C_D, is 11.240 for the front wing and

Table 4: Aerodynamic performance for different body components of the baseline aircraft in cruise. The fuselage C_L and C_D are normalized by $S_1 + S_2$.

Body	AR	C_L	C_D	C_L/C_D
FL	-	0.0162	0.0031	5.2929
FW	3.5	0.3778	0.0336	11.2404
RW	20	0.4501	0.0299	15.0611
TT	17.54	0.4308	0.0318	13.5544

15.061 for the rear wing, with an overall efficiency of $C_L/C_D = 13.554$ for the full aircraft. This design provides excellent aerodynamic efficiency based on conventional technology for low Reynolds number. However, the mission and weight analysis indicate that the low lift coefficient is not able to lift up the weight of its own empty structure excluding the batteries, solar panel, and scientific payloads in Martian atmosphere. The conventional technology is deemed not feasible to fly on Mars.

4.3 Performance with varying flow incidence

A flow incidence angle is introduced here to define the incoming flow relative to the designed cruise configurations presented in previous two subsections. It is not the angle of attack that is defined based on airfoil chord. The zero incidence is defined as the incoming flow direction aligned with the designed cruise flow direction. The incidence sign convention is the same as that for angle of attack.

An angle of incidence effect study was conducted on the MAGGIE aircraft designed with the DS-CFJ technology and the one with conventional airfoil NACA 6410 to evaluate their performance under unstable incoming flow conditions during cruise. The study examined angles of incidence (α) ranging from $-10°$ to $10°$ for both configurations, providing insights into the robustness and adaptability of the aircraft designs.

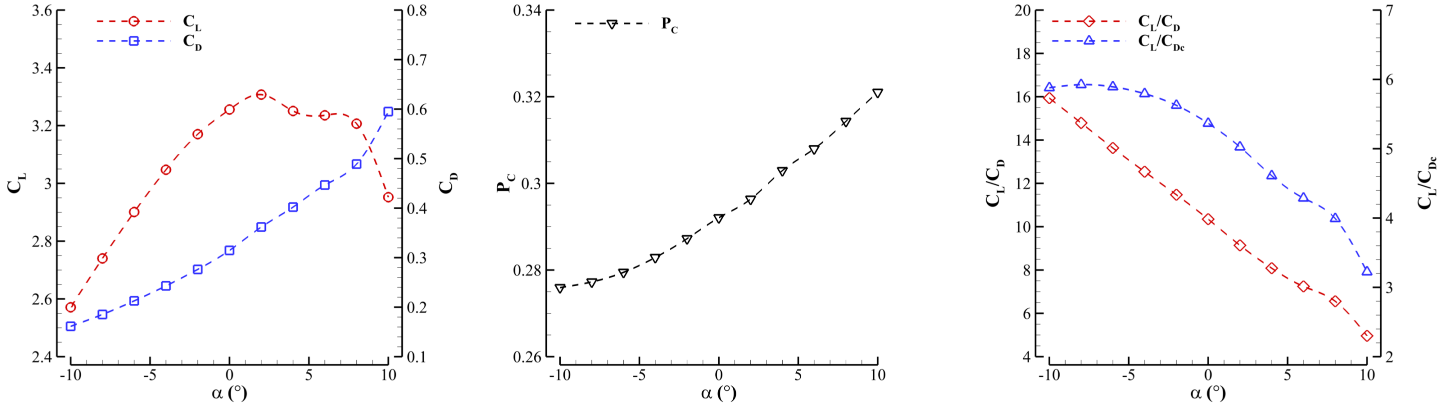

(a) (b) (c)

Figure 9: Aerodynamic performance of MAGGIE at different angle of incidence; (a) C_L and C_D; (b) power coefficient of the CFJ system P_C; (c) C_L/C_D and C_L/C_{Dc}.

Fig. 9 presents the aerodynamic performance of the MAGGIE aircraft at various angles of incidence. In Fig. 9 (a), the lift coefficient remains consistently high, ranging from 2.57 ($\alpha = -10°$) to 3.21 ($\alpha = 2°$), while the drag coefficient increases gradually with the angle of incidence, demonstrating MAGGIE's adaptability and reliability under cruise conditions. Fig. 9 (b) shows that the power coefficient required by the CFJ system increases with the angle of incidence, indicating higher energy demands at larger angles. Fig. 9 (c) highlights the aerodynamic efficiency (C_L/C_D) and corrected aerodynamic efficiency (C_L/C_{Dc}), with the maximum corrected efficiency of $C_L/C_{Dc} = 5.924$ achieved at $\alpha = -8°$. These results emphasize MAGGIE's efficient design and its ability to maintain excellent performance across a wide range of operational conditions.

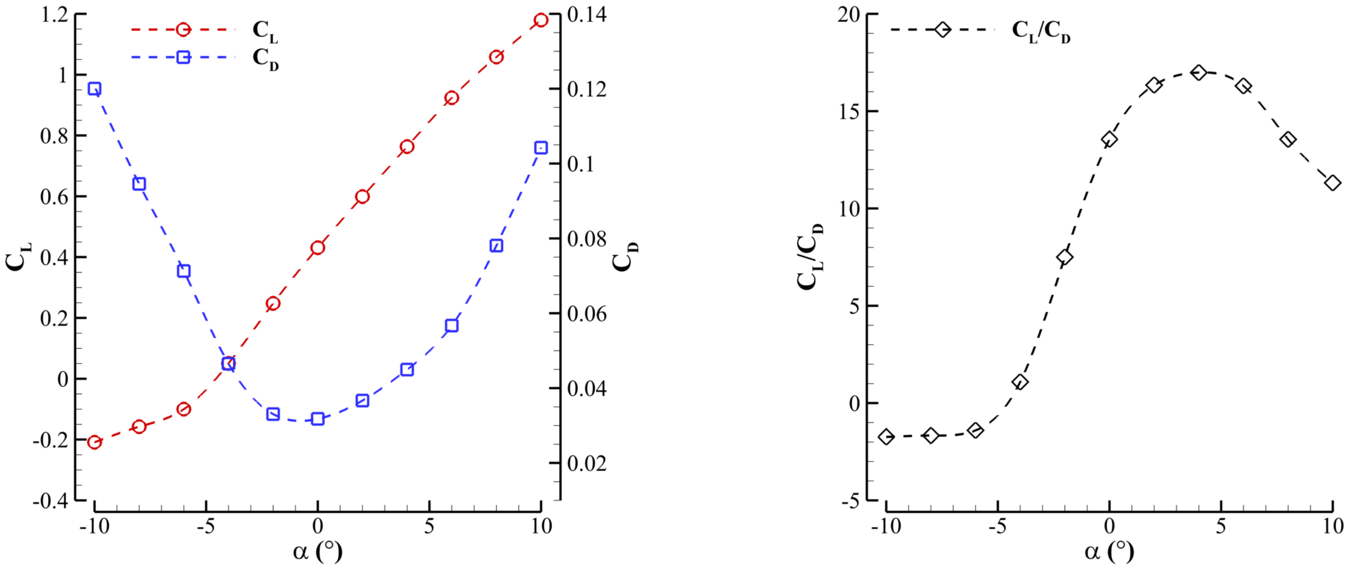

(a) (b)

Figure 10: Aerodynamic performance of the baseline aircraft at different angle of incidence; (a) C_L and C_D; (b) C_L/C_D.

Fig. 10 presents the aerodynamic performance of the baseline aircraft at various angles of incidence. In Fig. 10 (a), the lift coefficient increases with the angle of incidence, α, while the minimum drag occurs at $\alpha = 0°$. However, negative lift is observed when $\alpha < -6°$, which is undesirable during flight. Fig. 10 (b) illustrates the aerodynamic efficiency, represented as C_L/C_D, with a maximum value of $C_L/C_D = 16.98$ at $\alpha = 4°$. These results indicate a narrow operation range for the conventional configuration at cruise flight even though it is not feasible to perform flight mission on Mars.

5 Conclusions

The present study demonstrates the aerodynamic superiority and feasibility of a DS-CFJ powered tandem-wing aircraft (MAGGIE) for Martian cruise flight under ultra-low Reynolds number conditions. Numerical simulations reveal that the wing–wing interaction mechanism significantly enhances the overall aerodynamic performance, with the front wing benefiting from rear wing upwash and the rear wing gaining additional lift from front wing tip vortex influence. Despite localized flow separation near the rear wing suction surface just behind the front wing tip, the CFJ system maintains attached flow and high lift at large flap deflection angles. The optimized DS-CFJ configuration achieves a high lift coefficient of $C_L = 3.26$ and a corrected aerodynamic efficiency of $C_L/C_{D_c} = 5.37$, enabling sustained flight in the thin Martian atmosphere. In contrast, the baseline aircraft using conventional NACA 6410 airfoils yields insufficient lift ($C_L = 0.43$) despite high aerodynamic efficiency, rendering it incapable of supporting structural weight. Parametric studies with varying flow incidence further confirm MAGGIE's robustness and favorable performance margin. These findings validate the potential of DS-CFJ-enabled tandem-wing configurations as viable fixed-wing VTOL platforms for long-range, energy-sustainable Mars exploration.

6 Acknowledgment

This project is sponsored by NASA NIAC Grant Number 80NSSC24K0647. The numerical simulation of MAGGIE vehicle design and analysis is conducted with the computing resource of NASA High-End Computing systems. We greatly appreciate all the support from NASA.

References

[1] Y. Ren and G. Zha, "Performance enhancement by tandem wings interaction of coflow jet aircraft," in *AIAA Scitech 2021 Forum, AIAA Paper 2021-1823*.

[2] National Research Council, "Scientific Rationale for Mobility in Planetary Environments." Committee on Planetary and Lunar Exploration Space Studies Board, Commission on Physical Sciences, Mathematics, and Applications, 1999.

[3] M. D. Guynn, M. Croom, S. C. Smith, R. W. Parks, and R. W. Gelhausen, "Evolution of a Mars Airplane Concept for the ARES Mars Scout Mission ." AIAA Paper 2003-6578, Sept. 2003.

[4] NASA, "Mars aerial and ground global intelligent explorer, https://www.nasa.gov/general/mars-aerial-and-ground-global-intelligent-explorer," 2024. Accessed: 2025-06-20.

[5] R. E. Kuhn and J. W. Draper, "AN INVESTIGATION OF A WING-PROPELLER CONFIGURTION EMPLOYING LARGE-CHORD PLAIN FLAPS AND LARGE-DIAMETER PROPELLERS FOR LOW-SPEED FLIGHT AND VERTICAL TAKE-OFF ." NACA TN-3307, December 1954.

[6] R. E. Kuhn and J. W. Draper, "INVESTIGATION OF EFFECTIVENESS OF LARGE-CHORD SLOTTED FLAPS IN DEFLECTING PROPELLER SLIPSTREAMS DOWNWARD FOR VERTICAL TAKE-OFF AND LOW-SPEED FLIGHT ." NACA TN-3364, Jan. 1955.

[7] R. E. Kuhn, "Investigation of the Effects of Ground Proximity and Propeller Position on the Effectiveness of a Wing with Large-Chord Slotted Flaps in Redirecting Propeller Slipstreams Downward for Vertical Take-Off ." NACA TN-3629, March 1956.

[8] G.-C. Zha, "Feasibility Study of Deflected Slipstream Airfoil for VTOL Hover Enabled by CoFlow Jet." AIAA Paper 2023-4279, AIAA Aviation Forum 2023, San Diego, CA, 12-16 June 2023.

[9] K. R. Antcliff, S. K. Whiteside, L. W. Kohlman, and C. Silva, "Baseline Assumptions and Future Research Areas for Urban Air Mobility Vehicles." AIAA Paper 2019-0528, AIAA SciTech 2019 Forum, San Diego, CA, 7-11 January 2019.

[10] G. Zha, Y. Ren, and W. Fredericks, "Design and testing of deflected slipstream airfoil for vtol hover enabled by coflow jet," in *AIAA Paper 2024-4420, AIAA AVIATION FORUM AND ASCEND 2024*, p. 4420, 2024.

[11] Lefebvre, A. and Zha, G.-C. , "Design of High Wing Loading Compact Electric Airplane Utilizing Co-Flow Jet Flow Control." AIAA Paper 2015-0772, AIAA SciTech2015: 53nd Aerospace Sciences Meeting, Kissimmee, FL, 5-9 Jan 2015.

[12] Lefebvre, A. and Zha, G.-C., "Trade Study of 3D Co-Flow Jet Wing for Cruise and Takeoff/Landing Performance." AIAA Paper 2016-0570, AIAA SCITECH2016, AIAA Aerospace Science Meeting, San Diego, CA, 4-8 January 2016.

[13] Lefebvre, A. and Dano, B. and Bartow, W. and Di Franzo, M. and Zha, G.-C., "Performance Enhancement and Energy Expenditure of Co-Flow Jet Airfoil with Variation of Mach Number." AIAA Paper 2013-0490, AIAA Journal of Aircraft, DOI: 10.2514/1.C033113, 2016.

[14] Liu, Z.-X. and Zha, G.-C., "Transonic Airfoil Performance Enhancement Using Co-Flow Jet Active Flow Control." AIAA Paper 2016-3472, AIAA AVIATION 2016, 8th AIAA Flow Control Conference, Washington, D.C, June 13-17, 2016.

[15] Yang, Y.-C. and Zha, G.-C., "Super-Lift Coefficient of Active Flow Control Airfoil: What Is the Limit?." AIAA Paper 2017-1693, AIAA SCITECH2017, 55th AIAA Aerospace Science Meeting, Grapevine, Texas, 9-13 January 2017.

[16] G.-C. Zha, Y.-C. Yang, Y. Ren, and B. McBreen, "Super-lift and thrusting airfoil of coflow jet-actuated by micro-compressors." AIAA Paper 2017-3061, AIAA AVIATION 2018, Atlanta, GA , 25 - 29 June 2018.

[17] A. Smith, "High-Lift Aerodynamics," *Journal of Aircraft*, vol. 12, pp. 501–530, 1975.

[18] G.-C. Zha, "Estol performance for heavy lift transports using ultra-high lift high efficiency co-flow jet airfoil." Final Report to DARPA for Contract HR0011-16-2-0052, May 25, 2018.

[19] J. Boling and G.-C. Zha, " Numerical Investigation of Longitudinal Static Stability of a High-Speed Tandem-Wing VTOL Vehicle Using CoFlow Jet Airfoil." AIAA Paper 2021-1732, 2021 AIAA SciTech Virtual Forum, 15-19 June, 2020.

[20] B. McBreen and J. Boling and Y. Ren and and G.-C. Zha, "Variation of Moments for a Tailless High-Speed Tandem Wing VTOL Aircraft Using Distributed Propulsors and CoFlow Jets." AIAA Paper 2023-4282, AIAA AVIATION 2023 Forum, San Diego, CA, 12-16 June 2023.

[21] G.-C. Zha, W. Gao, and C. Paxton, "Jet Effects on Co-Flow Jet Airfoil Performance," *AIAA Journal, No. 6,*, vol. 45, pp. 1222–1231, 2007.

[22] Y. Wang and G.-C. Zha, "Study of 3D Co-flow Jet Wing Induced Drag and Power Consumption at Cruise Conditions." AIAA Paper 2019-0034, AIAA SciTech 2019, San Diego, CA, January 7-11, 2019.

[23] Y. Wang, Y.-C. Yang, and G.-C. Zha, "Study of Super-Lift Coefficient of Co-Flow Jet Airfoil and Its Power Consumption." AIAA Paper 2019-3652, AIAA Aviation 2019, AIAA Applied Aerodynamics Conference, Dallas, Texas, 17-21 June 2019.

[24] Y.-Q. Shen and G.-C. Zha, "Large Eddy Simulation Using a New Set of Sixth Order Schemes for Compressible Viscous Terms ," *Journal of Computational Physics*, vol. 229, pp. 8296–8312, 2010.

[25] Zha, G.C., Shen, Y.Q. and Wang, B.Y., "An improved low diffusion E-CUSP upwind scheme ," *Journal of Computer and Fluids*, vol. 48, pp. 214–220, Sep. 2011.

[26] Y.-Q. Shen and G.-Z. Zha , "Generalized finite compact difference scheme for shock/complex flowfield interaction," *Journal of Computational Physics*, vol. doi:10.1016/j.jcp.2011.01.039, 2011.

[27] Shen, Y.-Q. and Zha, G.-C. and Wang, B.-Y., " Improvement of Stability and Accuracy of Implicit WENO Scheme," *AIAA Journal*, vol. 47, No. 2, pp. 331–344, 2009.

[28] Shen, Y.-Q. and Zha, G.-C. and Chen, X.-Y., " High Order Conservative Differencing for Viscous Terms and the Application to Vortex-Induced Vibration Flows," *Journal of Computational Physics*, vol. 228(2), pp. 8283–8300, 2009.

[29] Shen, Y.-Q. and Zha, G.-C. , " Improvement of the WENO Scheme Smoothness Estimator," *International Journal for Numerical Methods in Fluids*, vol. DOI:10.1002/fld.2186, 2009.

[30] G.-C. Zha and E. Bilgen, "Numerical Study of Three-Dimensional Transonic Flows Using Unfactored Upwind-Relaxation Sweeping Algorithm," *Journal of Computational Physics*, vol. 125, pp. 425–433, 1996.

[31] B.-Y. Wang and G.-C. Zha, "A General Sub-Domain Boundary Mapping Procedure For Structured Grid CFD Parallel Computation," *AIAA Journal of Aerospace Computing, Information, and Communication*, vol. 5, No.11, pp. 2084–2091, 2008.

[32] Y.-Q. Shen, G.-C. Zha, and B.-Y. Wang, "Improvement of Stability and Accuracy of Implicit WENO Scheme ," *AIAA Journal*, vol. 47, pp. 331–344, 2009.